energies

Article

Enhanced Primary Frequency Control Using Model Predictive Control in Large-Islanded Power Grids with High Penetration of DFIG-Based Wind Farm

Youssef Ait Ali [1], Mohammed Ouassaid [1], Zineb Cabrane [1,2] and Soo-Hyoung Lee [3,*]

1 Engineering for Smart and Sustainable Systems Research Center, Mohammadia School of Engineers, Mohammed V University in Rabat, Rabat 10090, Morocco; youssef_aitali@um5.ac.ma (Y.A.A.); ouassaid@emi.ac.ma (M.O.); zinebcabrane@gmail.com (Z.C.)
2 Laboratory of Innovative Technologies, National School of Applied Sciences of Tangier, Abdelmalek Essaadi University, Tetouan 93000, Morocco
3 Department of Electrical and Control Engineering, Mokpo National University, Mokpo 58554, Republic of Korea
* Correspondence: slee82@mokpo.ac.kr

Abstract: A new primary frequency controller in power grids undergoing massive wind power penetration is the focus of this paper. The inescapable problem in a largely wind penetrated power grid is to ensure the maintenance of its frequency in the nominal band prescribed by the power system operator (PSO). However, with the massive arrival of wind farms with conventional control schemes, the operation of maintaining and restoring the frequency to the regulatory regimes remains very complicated. In order to overcome the above problem, this paper proposes a new strategy for primary frequency control in power grids using model predictive control (MPC) for a multi-cluster doubly-fed induction generator (DFIG)-based wind farm (WF), with a main objective of reducing the frequency nadir (FN), eliminating the second frequency dip (SFD), and providing the optimal support during wind speed variations. In this approach, a rolling prediction and optimization control strategy is developed based on the dynamic power system model to ideally predict the additional power to be provided. Moreover, in order to avoid second frequency dips, the wind turbines (WTs) are not allocated to extract additional power from the grid during the frequency event, the rotor speeds are not recovered to the maximum power point tracking (MPPT) operating points during the primary frequency control. The performance of the proposed controller was evaluated using a two-zone electrical system in MATLAB/Simulink®. The obtained results disclose that the frequency nadir is enhanced with more than 6.1% compared to the conventional schemes. In addition, the frequency response settling time has been improved with more than 10.51 s.

Keywords: power grid; primary frequency control; DFIG-based wind farm; inertial control; predictive control

Citation: Ali, Y.A.; Ouassaid, M.; Cabrane, Z.; Lee, S.-H. Enhanced Primary Frequency Control Using Model Predictive Control in Large-Islanded Power Grids with High Penetration of DFIG-Based Wind Farm. *Energies* **2022**, *16*, 4389. https://doi.org/10.3390/en16114389

Academic Editor: Anca D. Hansen

Received: 24 April 2023
Revised: 17 May 2023
Accepted: 21 May 2023
Published: 29 May 2023

1. Introduction

Over the past few decades, a massive influx of large wind farms has taken place all over the world, and huge offshore wind farms have been especially integrated into power grids [1]. This introduces more and more adverse effects on the stability of the power system. One of the toughest issues faced is the impact of wind power generation on frequency control.

1.1. Literature Review

Power frequency control for wind farms so that they can be connected to the grid is a fundamental requirement in most countries around the world [2,3]. In the United Kingdom, the PSO requires a frequency droop in the 3 and 5% band for primary frequency control, while in Canada, a minimum 10% increase in active power during frequency events is required by the Independent Electricity System Operator. In Denmark, wind farms are required to adjust their output in the range of 10 to 100% during power events. EirGrid in Ireland requires a 15% reduction in active power during over-frequency events [2].

The literature review shows that a variety of research works have suggested a multitude of control strategies emulating the natural inertia of synchronous generators in WTs in order to mitigate frequency fluctuations during the most severe power system events. Indeed, studies in [4,5] have pointed out the rate of change of frequency (ROCOF) is significantly reduced by WT providing emulated inertial response. It is also shown that inertia emulation in WTs and droop control result in lower FN and faster recovery of the established frequency regime [6,7]. A combined control action of inertia emulation and the droop control method significantly improves the frequency response [8,9].

To achieve the contribution to frequency control, WTs increase or decrease their power outputs. This is achieved by operating the wind turbine in a deloaded operating point by reducing its pitch angle [3,7–10]. Meanwhile, this technique is recommended only for small and medium-sized wind turbines since the actuator time constant becomes large with increasing generator size, which adversely affects the frequency response. Thus, other studies have proposed to operate WTs at both suboptimal speed points [11,12]. Practically, frequency controllers based on wind turbine speed control have been shown to provide faster responses to system frequency [13]. However, all of these techniques introduce considerable loss given that they continuously operate generators at suboptimal points even before the frequency event. This means that the cash flow of the PSO is severely impaired.

In the same impetus, classical proportional integral (PID) and fractional order control have been proposed for angle of attack tuning and to improve the frequency response [14,15]. Fuzzy logic has also been used to solve the primary frequency tuning problem [16,17], but the results are highly dependent on the controller parameter settings. In addition, the studies in [18,19] develop a model predictive scheme to control the active power of the WF participating in primary frequency control. The development has been extended to a highly simplified power grid model that does not consider all elements of the power system. In the same perspective, interesting results have been obtained in [20,21], these studies used metaheuristic algorithms to build an optimized virtual rotor controller for energy systems connected to islanded microgrids. Table 1 synthesizes the strengths and weaknesses of the proposed control strategies in the literature.

Table 1. Control strategies for primary frequency control comparison.

Control	Advantages	Disadvantages	SFD Consideration	Ref
Inertial control	- Easy to implement. - Low computation rate.	- Dependence of the ROCOF and K_{in}. - Slow response.	No	[22] [23]
Droop control	- Easy to implement. - Low computation rate.	- Dependence of the Droop and K_D. - Slow response.	No	[7] [24] [25] [26]
Combined control & Variable Droop	- Easy to implement. - Low computation rate.	- Dependence of the ROCOF and Droop. - Tuning of K_D and K_{in} is mandatory.	No	[12] [27] [28] [29]
PID-Fuzzy	- Relatively easy to implement. - Moderated computation rate.	- Tuning of K_P and K_I is mandatory. - Hard definition of control rules.	No	[30] [31]

Table 1. *Cont.*

Control	Advantages	Disadvantages	SFD Consideration	Ref
Fuzzy Logic	- Relatively easy to implement. - Moderated computation rate.	- Tuning of K_P and K_I is mandatory. - Hard definition of control rules.	No	[17] [32] [33] [34]
MPC Control	- The consideration of control constraints. - The output is optimally calculated.	- Advanced level of control difficulty. - Heavy computations are involved.	Yes	Proposed

1.2. Research Motivations

To design an optimal controller to addresses the drawbacks discussed in the literature review, it is legitimate to think of a control law producing an optimal output from a minimization of the quadratic cost function based on the dynamic model of the multi-zone power system and with various clusters of WTs operating at different wind speeds. The MPC technique considers the constraints on the output frequency deviation and load variation to compute the optimal control signal, as well as the constraints on the control signal. Indeed, a fast control strategy to increase the FN near the settlement frequency while ensuring the stable operation of the DFIG-based WTS under varying wind and load conditions is the objective of this paper. This objective is achieved through a novel MPC-based control scheme in which speeds are not rolled back to MPPT operating points during the primary frequency event support. The MPC controller measures the frequency deviation Δf as an input and calculates the additional power based on the spatial state model of the power system frequency response. When the frequency stabilizes, Δf does not cancel, the controller prevents the speed from recovering. In fact, the DFIG speed automatically recovers when the frequency is in its nominal band during the secondary frequency control; therefore, the MPC-based frequency control releases more deceleration kinetic energy compared to the generic control strategies. In addition, the FN in the proposed MPC control scheme is increased to be close to the establishment frequency without worrying about the SFD.

1.3. Contribution and Paper Organization

The main contributions of the proposed MPC-based fast frequency control are summarized as follows:

- The FN is improved with more than 6.1% to be close to the settling frequency under all clusters wind and overload conditions, without SFD. This has never been achieved with existing conventional schemes, to our knowledge.
- In order to meet the PSO requirements, the stabilization time to reach the new steady state frequency is significantly improved. It has been improved by more than 10.51 s compared to conventional schemes.
- No electrical energy is required by the WTs to return the rotational speeds to the MPPT operating points during the frequency event, which positively improves the behavior of the power system with the proposed controller.

The remainder of this paper is structured as follows: Section 2 illustrates the theoretical modeling of the WTs, Section 3 details the proposed controller, In Section 4, the obtained results are discussed. Finally, Section 5 summarizes the conclusion.

2. Model of a DFIG-Based WT

2.1. Wind Turbine Model

The output power of a WT is expressed as follows [29]:

$$P_m = \frac{1}{2}\rho A C_p(\lambda, \beta) V_\omega^3 \quad (1)$$

where ρ is the air density (in kg/m^3) and A is the section formulated by the turbine blades (in m^2). The power conversion coefficient, denoted by C_p, is a function of two variables: the turbine pitch angle, measured in degrees, and the tip–speed ratio (TSR). The expression for λ is given by:

$$\lambda = \frac{\omega_r R}{V_\omega} \quad (2)$$

The parameters ω_r and R represent, respectively, the rotational speed of the shaft (in rad/s), and the radius formed by the turbine blades (in m). The power conversion coefficient C_p is a nonlinear function of the turbine pitch angle (in degrees) and the tip–speed ratio λ, which is defined as the ratio of the speed of the blade tips to the speed of the wind that drives them. It is noteworthy that the coefficient C_p has a specific maximum value at a particular tip–speed ratio λ_{Opt}.

To characterize the performance of a wind turbine, a generalized equation is employed to model the power conversion coefficient $C_p(\lambda, \beta)$. This equation is expressed as follows:

$$C_p(\lambda, \beta) = c_1\left(\frac{c_2}{\lambda_i} - c_3\beta - c_4\right)e^{\left(-\frac{c_5}{\lambda_i}\right)} + c_6\lambda \quad (3)$$

$$\frac{1}{\lambda_i} = \frac{1}{\lambda + 0.08\beta} - \frac{0.035}{\beta^3 + 1}$$

where c_1, c_2, c_3, c_4, c_5, c_6 represent the WT's manufacturer aerodynamic power coefficients.

In order to extract the optimal power that can be served by the WTs for given wind conditions, the speed controller operates with the MPPT characteristic depicted in Figure 1, which can be expressed by Equation (5), where K_{Opt} is the optimal coefficient for the MPPT, whose value is given in Table A3.

According to the characteristic in Figure 1, the segment $A - B$ aligns with the starting zone, and the turbine is engaged in this zone. In the segment $B - C$, which is called the optimal zone, the controller adjusts the rotational speed by regulating DFIG$'$ rotor current, and then modifies the power extracted from the turbine. Finally, in the $C - D$ segment, the speed is maintained nearly unchanged until the power attains its rated value. Beyond point D, the generator can no longer increase its power for protection reasons, and the pitch angle controller performs control maneuvers, which saturates the power output.

$$P_m = \begin{cases} \frac{K_{Opt}\omega_0^3}{(\omega_0 - \omega_{rmin})}(\omega_r - \omega_{rmin}) & , \omega_{rmin} \leq \omega_r < \omega_0 \\ K_{Opt}\omega_r^3 & , \omega_0 \leq \omega_r \leq \omega_1 \\ \frac{P_{max} - K_{Opt}\omega_1^3}{(\omega_{rmax} - \omega_1)}(\omega_r - \omega_{rmax}) & , \omega_1 < \omega_r \leq \omega_{rmax} \end{cases} \quad (4)$$

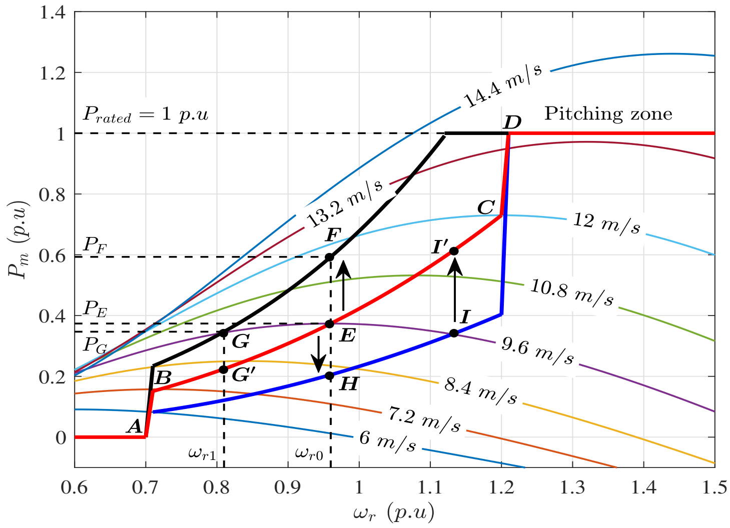

Figure 1. WT power characteristics with $\beta = 0°$ and at different wind speeds; bold red (MPPT curve), bold blue and black (Shifted optimal power point tracking (OPPT) curves).

2.2. Power Reserve Deployment Requirements for Primary Frequency Control

Figure 2 portrays the basis of power system frequency behavior following a sudden loss of energy production or following an overloading event; it also illustrates the involved energy reserve levels. The grid frequency begins to drop, and only the instantaneous inertia reserves of the synchronous generators can renew the power balance in the system. Once a specific activation frequency is attained, the primary power reserves are triggered, this escalates the mechanical power of the generators until a different balance between the required electrical power and the generated mechanical power is reached. At this point, the frequency stops falling, it stabilizes on a new threshold below its nominal value.

Moreover, the FN and settling frequency are greatly determined by the slope of the frequency droop characteristic [35,36], the slower the response of the synchronous generator controller, the lower the FN.

The deployment of the secondary reserves rectifies the frequency levels to standard operational parameters, which triggers the deactivation of the primary reserves. The secondary reserves are implemented until they are wholly taken over by the tertiary reserves.

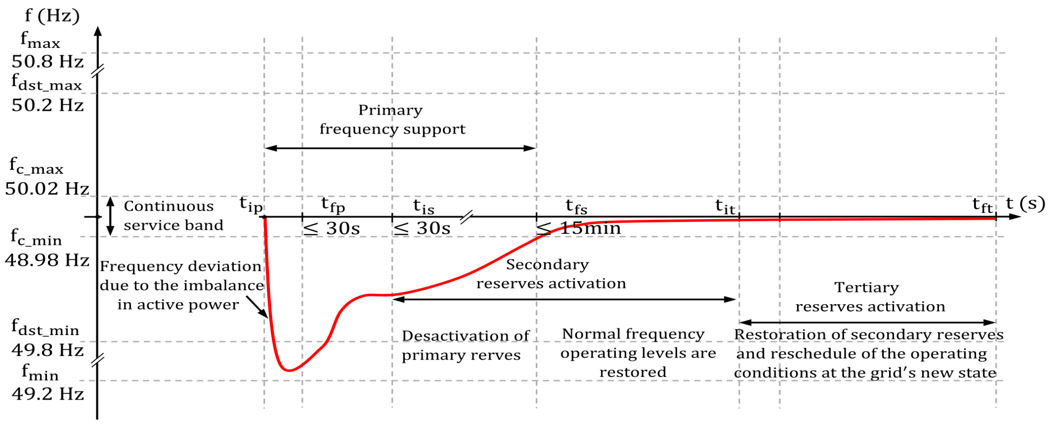

Figure 2. Concepts definition (The designated values for time frames and frequencies comply with the recommendations of ENTSO-E) [37].

2.3. Emulation of Inertial Response in a DFIG-Based WT

It is possible that a DFIG-based WTS emulates the inertial response of traditional synchronous generators, since each rotating mass generates kinetic energy as it decelerates. To reach this target, it is essential to make some modifications to control scheme. In the aerodynamic characteristic of the DFIG-based WTS depicted in Figure 1, if the WT is only governed by the MPPT control curve and then an underfrequency event happens (e.g., due to a sudden overloading in the power grid or by loss of a generation unit); the conventional SGs are then called to raise their power production by making use of the primary energy reserves available—this will result in reducing the imbalance between the requested active power and the produced power.

The PSO requirements require WTS to participate in supporting grid contingencies; they are required to increase their output active power by moving immediately from the MPPT operating point located at E, to somewhere around point F in the left shifted MPPT as shown in Figure 1. Operating at point F will support the demand in active power and reduce the suffered imbalance. The active power demanded in F exceeds the mechanical power that can be delivered by the WT for the actual wind conditions; this will trigger rotor deceleration to the equilibrium point G $(\omega_{r0} \rightarrow \omega_{r1})$. Throughout the ($E$–$F$–$G$) operation process, the DFIG-WT has been giving away a portion of its stored kinetic energy to reduce the FN. Although, going forward, it is working at a sub-optimal point G; the process of recovering the active power reference signal to its maximum point P_E will occur during the secondary frequency regulation, passing by $P_{G'}$. Likewise, during the over-frequency event, the DFIG-WT inertial response describes the path (E–H–I–I'), except that this time, the rotor speed is restored to the MPPT point E directly at the end of the frequency disturbance.

It is infeasible to limit the deviation between the FN and the settling frequency if only the MPPT controller is operated. This is due to the fact that the speed recovery inevitably consumes additional energy from power grid to accelerate the turbine into MPPT point. In the MPC-based frequency control strategy, the FN is raised closer to the settling frequency since no speed recovery is allocated.

In the additional Δf loop proposed in [38,39], the frequency responses remain limited. For good results, the MPPT and Δf components are combined in the MPC-based frequency control strategy. Indeed, with the MPPT curve, the power reference will moderately decrease with the DFIG-WT deceleration, making the DFIG-WT behavior sufficiently stable. As depicted in Figure 1, during frequency support, the OPPT power curve used for limitation decreases with ω_r from point F to point G. When supporting the frequency in the F–G segment, the controller inherits MPPT proprieties, it has the privilege to adapt its operating point if the wind conditions change.

The analysis conducted above shows that the proposed controller allows the WTS power to decrease and stabilize smoothly at the power point G without introducing oscillations in the power system frequency, which cannot be provided by conventional SGs with highly oscillating characteristics.

3. Model Predictive Control for DFIG Supporting Frequency Control

3.1. DFIG Model

In stator voltage oriented control, the d axis of the dq reference frame is selected to carry the mains voltage vector $\overrightarrow{v_s}$, and the rotating reference frame dq, rotates at the synchronous speed ω_s of the stator voltage. The DFIG dynamic equations are given by [40,41]:

$$\begin{cases} v_s^k(t) = R_s i_s^k(t) + \dfrac{d}{dt}\phi_s^k(t) + \omega_s(t)\boldsymbol{J}\phi_s^k(t) \\ v_r^k(t) = R_r i_r^k(t) + \dfrac{d}{dt}\phi_r^k(t) + \omega_{sl}(t)\boldsymbol{J}\phi_r^k(t) \end{cases} \quad (5)$$

where, $\boldsymbol{J} = \begin{bmatrix} 0 & -1 \\ 1 & 0 \end{bmatrix}$, $\omega_{sl}(t) = \omega_s(t) - \omega_r(t)$ is the angular sliding pulsation, the vector $x^k(t)$ denotes the dq attributes of each variable, it is given by $x^k = (x^d, x^q)^T$.

The stator and rotor flux linkages are represented as [40,41]:

$$\begin{cases} \phi_s^k(t) = L_s i_s^k(t) + L_m i_r^k(t) \\ \phi_r^k(t) = L_r i_r^k(t) + L_m i_s^k(t) \end{cases} \tag{6}$$

The magnitude of the stator voltage d-axis component v_s^d is identical to v_s while the q-axis element v_s^q is constantly maintained at zero, $v_s^d(t) = ||v_s(t)||$ and $v_s^q(t) = 0$. The replacement of the value of $\phi_r^k(t)$ from Equation (6) to Equation (5) results in the expression of the rotor voltages as $v_r^k(t)$, as shown in Equation (7).

$$v_r^k(t) = R_r i_r^k(t) + \sigma L_r \frac{d}{dt} i_r^k(t) + \frac{L_m}{L_s}\frac{d}{dt}\phi_s^k(t) + \omega_{sl}(t)\sigma L_r \boldsymbol{J} i_r^k(t) + \omega_{sl}(t)\frac{L_m}{L_s}\boldsymbol{J} i_s^k(t) \tag{7}$$

where $\sigma = 1 - \dfrac{L_m^2}{L_s L_r}$ represents the DFIG leakage coefficient.

The expressions for the derivatives of the rotor currents are obtained in Equation (8). This is achieved with the aim of achieving current control.

$$\begin{cases} \frac{d}{dt} i_r^d(t) = \frac{1}{\sigma L_s L_r}\left[-R_r L_s i_r^d(t) + (\omega_{sl}(t) L_s L_r - \omega_s(t) L_m^2) i_r^q(t) + R_s L_m i_s^d(t) - \omega_r(t) L_m L_s i_s^q(t) + L_s v_r^d(t) - L_m v_s^d(t)\right] \\ \frac{d}{dt} i_r^q(t) = \frac{1}{\sigma L_s L_r}\left[-R_r L_s i_r^q(t) + (\omega_{sl}(t) L_s L_r - \omega_s(t) L_m^2) i_r^d(t) + R_s L_m i_s^q(t) + \omega_r(t) L_m L_s i_s^d(t) + L_s v_r^q(t) - L_m v_s^q(t)\right] \end{cases} \tag{8}$$

The DFIG's rotor currents can be acquired directly from Equation (9) [42].

$$\begin{cases} i_r^d(t) = -\frac{2}{3}\frac{L_s}{L_m v_s^d(t)} P_s(t) \\ i_r^q(t) = \frac{2}{3}\frac{L_s}{L_m v_s^d(t)} Q_s(t) - \frac{v_s^d(t)}{\omega_s(t) L_m} \end{cases} \tag{9}$$

where, $P_s(t)$ and $Q_s(t)$ denote the DFIG's active and reactive powers, respectively.

3.2. RL Filter and Inverter Models

In the dq rotating frame, the RL filter model can be written as follows [42]:

$$v_s^k(t) = R_f i_f^k(t) + L_f \frac{d}{dt} i_f^k(t) + \omega_s(t) L_f \boldsymbol{J} i_f^k(t) + v_f^k(t) \tag{10}$$

The expressions for the derivatives of the filter current are derived in Equation (11).

$$\begin{cases} \frac{d}{dt} i_f^d(t) = \left[-\frac{R_f}{L_f} i_f^d(t) + \omega_s(t) i_f^q(t) + \frac{1}{L_f}(v_s^d(t) - v_f^d(t))\right] \\ \frac{d}{dt} i_f^q(t) = \left[-\frac{R_f}{L_f} i_f^d(t) - \omega_s(t) i_f^d(t) + \frac{1}{L_f}(v_s^q(t) - v_f^q(t))\right] \end{cases} \tag{11}$$

In the insulated-gate bipolar transistor (IGBT)-based three-phase voltage inverter illustrated in Figure 3, current can flow in both directions through six bi-directional switches (that can be controlled to be on or off) and anti-parallel diodes. All components are treated as ideal switches.

The switch states allow for expressing the voltages as:

$$\begin{bmatrix} v_{an} \\ v_{bn} \\ v_{cn} \end{bmatrix} = \frac{v_{dc}}{3}\begin{bmatrix} 2 & -1 & -1 \\ -1 & 2 & -1 \\ -1 & -1 & 2 \end{bmatrix}\begin{bmatrix} S_a \\ S_b \\ S_c \end{bmatrix} \tag{12}$$

By coding the possible switching of the IGBT switches using three states (S_a, S_b, S_c), it becomes feasible to determine the voltage vector obtained in the stationary frame (α, β) for a particular switch combination. This information is then used to construct the switching polygon as depicted in Figure 4.

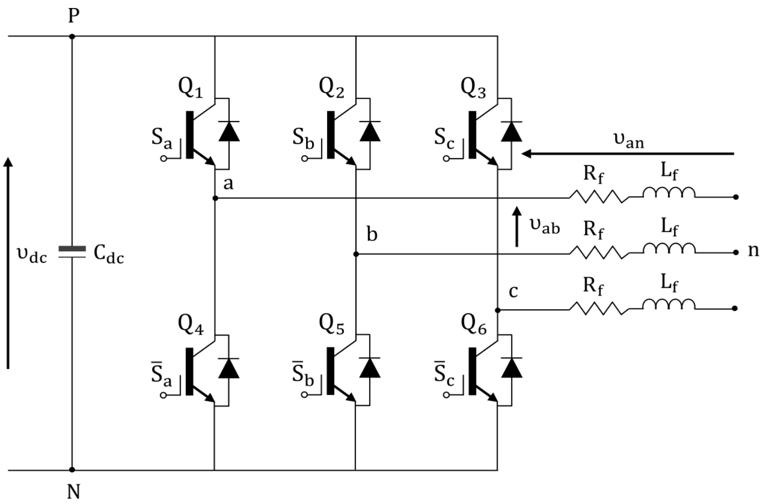

Figure 3. Structure of the three-phase voltage source inverter.

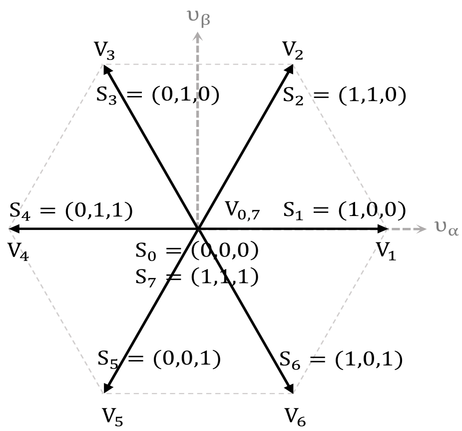

Figure 4. Switching pattern of the three-phase voltage source inverter.

3.3. Finite Control Set-Model Predictive Control (FCS-MPC) for DFIG-Based Wind Turbine

The direct Euler in Equation (13) discrete-time model is employed for predicting currents in the future sampling periods [42,43]. The DFIG $P + P^2$ FCS-MPC discrete model at the first future sampling period can be expressed as illustrated in Equations (14) and (15) [42]:

$$\left[\frac{d}{dt}x(t)\right]_{t=t_k} \approx \boldsymbol{A}x(t_k) + \boldsymbol{B}u(t_k) = \frac{x(t_{k+1}) - x(t_k)}{T_s} \tag{13}$$

$$\begin{aligned}\begin{bmatrix} i_r^d(t_{k+1}) \\ i_r^q(t_{k+1}) \end{bmatrix} = \begin{bmatrix} 1 & 0 \\ 0 & 1 \end{bmatrix}\begin{bmatrix} i_r^d(t_k) \\ i_r^q(t_k) \end{bmatrix} + T_s \begin{bmatrix} -\dfrac{R_r}{\sigma L_s L_r} & \dfrac{\omega_{sl}(t_k)L_s L_r - \omega_s(t_k)L_m^2}{L_s L_r} \\ -\dfrac{\omega_{sl}(t_k)L_s L_r - \omega_s(t_k)L_m^2}{L_s L_r} & -\dfrac{R_r}{\sigma L_s L_r} \end{bmatrix}\begin{bmatrix} i_r^d(t_k) \\ i_r^q(t_k) \end{bmatrix} \\ + \frac{T_s}{\sigma L_s L_r}\begin{bmatrix} R_s L_m & -\omega_r(t_k)L_m L_s \\ \omega_r(t_k)L_m L_s & R_s L_m \end{bmatrix} + \frac{T_s}{\sigma L_r}\begin{bmatrix} v_r^d(t_k) \\ v_r^q(t_k)- \end{bmatrix} - \frac{T_s L_m}{\sigma L_r}\begin{bmatrix} v_s^d(t_k) \\ v_s^q(t_k) \end{bmatrix}\end{aligned} \tag{14}$$

$$\begin{bmatrix} i_f^d(t_{k+1}) \\ i_f^q(t_{k+1}) \end{bmatrix} = \begin{bmatrix} 1 & 0 \\ 0 & 1 \end{bmatrix}\begin{bmatrix} i_f^d(t_k) \\ i_f^q(t_k) \end{bmatrix} + T_s \begin{bmatrix} -\dfrac{R_f}{L_f} & \omega_s(t_k) \\ -\omega_s(t_{k+1}) & -\dfrac{R_f}{L_f} \end{bmatrix}\begin{bmatrix} i_f^d(t_k) \\ i_f^q(t_k) \end{bmatrix} + \frac{T_s}{L_f}\begin{bmatrix} v_s^d(t_k) \\ v_s^q(t_k) \end{bmatrix} - \frac{T_s}{L_f}\begin{bmatrix} v_f^d(t_k) \\ v_f^q(t_k) \end{bmatrix} \tag{15}$$

The model expressed by Equations (14) and (15) predicts the behavior of the DFIG rotor currents at a single sampling time, these values are reproduced in the discrete model to obtain the responses of the currents at two future sampling periods, the final model is expressed by Equations (16) and (17) [42].

$$\begin{bmatrix} i_r^d(t_{k+2}) \\ i_r^q(t_{k+2}) \end{bmatrix} = \begin{bmatrix} 1 & 0 \\ 0 & 1 \end{bmatrix} \begin{bmatrix} i_r^d(t_{k+1}) \\ i_r^q(t_{k+1}) \end{bmatrix} + T_s \begin{bmatrix} -\dfrac{R_r}{\sigma L_s L_r} & \dfrac{\omega_{sl}(t_{k+1}) L_s L_r - \omega_s(t_{k+1}) L_m^2}{L_s L_r} \\ -\dfrac{\omega_{sl}(t_{k+1}) L_s L_r - \omega_s(t_{k+1}) L_m^2}{L_s L_r} & -\dfrac{R_r}{\sigma L_s L_r} \end{bmatrix} \begin{bmatrix} i_r^d(t_{k+1}) \\ i_r^q(t_{k+1}) \end{bmatrix} + \frac{T_s}{\sigma L_s L_r} \begin{bmatrix} R_s L_m & -\omega_r(t_{k+1}) L_m L_s \\ \omega_r(t_{k+1}) L_m L_s & R_s L_m \end{bmatrix} + \frac{T_s}{\sigma L_r} \begin{bmatrix} v_r^d(t_{k+1}) \\ v_r^q(t_{k+1}) - \end{bmatrix} - \frac{T_s L_m}{\sigma L_r} \begin{bmatrix} v_s^d(t_{k+1}) \\ v_s^q(t_{k+1}) \end{bmatrix} \tag{16}$$

$$\begin{bmatrix} i_f^d(t_{k+2}) \\ i_f^q(t_{k+2}) \end{bmatrix} = \begin{bmatrix} 1 & 0 \\ 0 & 1 \end{bmatrix} \begin{bmatrix} i_f^d(t_{k+1}) \\ i_f^q(t_{k+1}) \end{bmatrix} + T_s \begin{bmatrix} -\dfrac{R_f}{L_f} & \omega_s(t_{k+1}) \\ -\omega_s(t_{k+1}) & -\dfrac{R_f}{L_f} \end{bmatrix} \begin{bmatrix} i_f^d(t_{k+1}) \\ i_f^q(t_{k+1}) \end{bmatrix} + \frac{T_s}{L_f} \begin{bmatrix} v_s^d(t_{k+1}) \\ v_s^q(t_{k+1}) \end{bmatrix} - \frac{T_s}{L_f} \begin{bmatrix} v_f^d(t_{k+1}) \\ v_f^q(t_{k+1}) \end{bmatrix} \tag{17}$$

Extrapolations to a single and two sampling steps use Equations (18) and (19) [42].

$$i_{ref}^k(t_{k+1}) = 3 i_{ref}^k(t_k) - 3 i_{ref}^k(t_{k-1}) + i_{ref}^k(t_{k-2}) \tag{18}$$

$$i_{ref}^k(t_{k+2}) = 6 i_{ref}^k(t_k) - 8 i_{ref}^k(t_{k-1}) + 3 i_{ref}^k(t_{k-2}) \tag{19}$$

The best switching state is obtained by minimizing the objective function given in Equation (20). The first part of g represents the currents absolute error, while the second eliminates switching states resulting in exceeding the rated current of DFIG. The third term reduces the switching frequency of power converters. The term λ_{sw} is set to 3.8×10^{-7} for the RSC and $\lambda_{sw} = 1.5 \times 10^{-7}$ for the GSC [42].

Algorithm 1 and Figure 5 depict the proposed control scheme.

$$g_{RSC,GSC} = |i_{ref}^d(t_{k+2}) - i_p^d(t_{k+2})| + |i_{ref}^q(t_{k+2}) - i_p^q(t_{k+2})| + \begin{cases} 0 & \text{if } \sqrt{i_p^d(t_{k+2})^2 + i_p^q(t_{k+2})^2} \le i_{max} \\ +\infty & \text{if } \sqrt{i_p^d(t_{k+2})^2 + i_p^q(t_{k+2})^2} > i_{max} \end{cases} + \lambda_{sw} \sum_{x=a,b,c} (S_x^p(t_k) - S_x^{opt}(t_k)) \tag{20}$$

Algorithm 1 FCS-MPC Rotor Currents Regulation Algorithm.

MEASUREMENT $(\mathbf{x_r^{k*}}(\mathbf{t_k}), \mathbf{x_f^{k*}}(\mathbf{t_k}))$
EXTRAPOLATION $(\mathbf{x_r^{k*}}(\mathbf{t_{k+2}}), \mathbf{x_f^{k*}}(\mathbf{t_{k+2}}))$
  $(\mathbf{x_r^{k*}}(\mathbf{t_{k+2}}), \mathbf{x_f^{k*}}(\mathbf{t_{k+2}})) \leftarrow$ **Equation** (19).
MEASUREMENT $(\mathbf{x_r^{k}}(\mathbf{t_k}), \mathbf{x_f^{k}}(\mathbf{t_k}))$
PREDICTION $(\mathbf{x_r^{kp}}(\mathbf{t_{k+2}}), \mathbf{x_f^{kp}}(\mathbf{t_{k+2}}))$
  for i = 1,. . . ,7
  $(\mathbf{x_r^{kp}}(\mathbf{t_{k+2}}) \mid \mathbf{x_f^{kp}}(\mathbf{t_{k+2}})) \leftarrow$ (Equation (16) | Equation (17)).
  $(\mathbf{g_{i-RSC}} \mid \mathbf{g_{i-GSC}}) \leftarrow$ (Equation (20)).
  end
  $\mathbf{f_{sw-RSC}}(\mathbf{t_k}) \leftarrow min[\mathbf{g_{i-RSC}}]_{i=1,2,\ldots,7}$
  $\mathbf{f_{sw-GSC}}(\mathbf{t_k}) \leftarrow min[\mathbf{g_{i-GSC}}]_{i=1,2,\ldots,7}$
RETURN $\mathbf{f_{sw-RSC}}(\mathbf{t_k}), \mathbf{f_{sw-GSC}}(\mathbf{t_k})$.

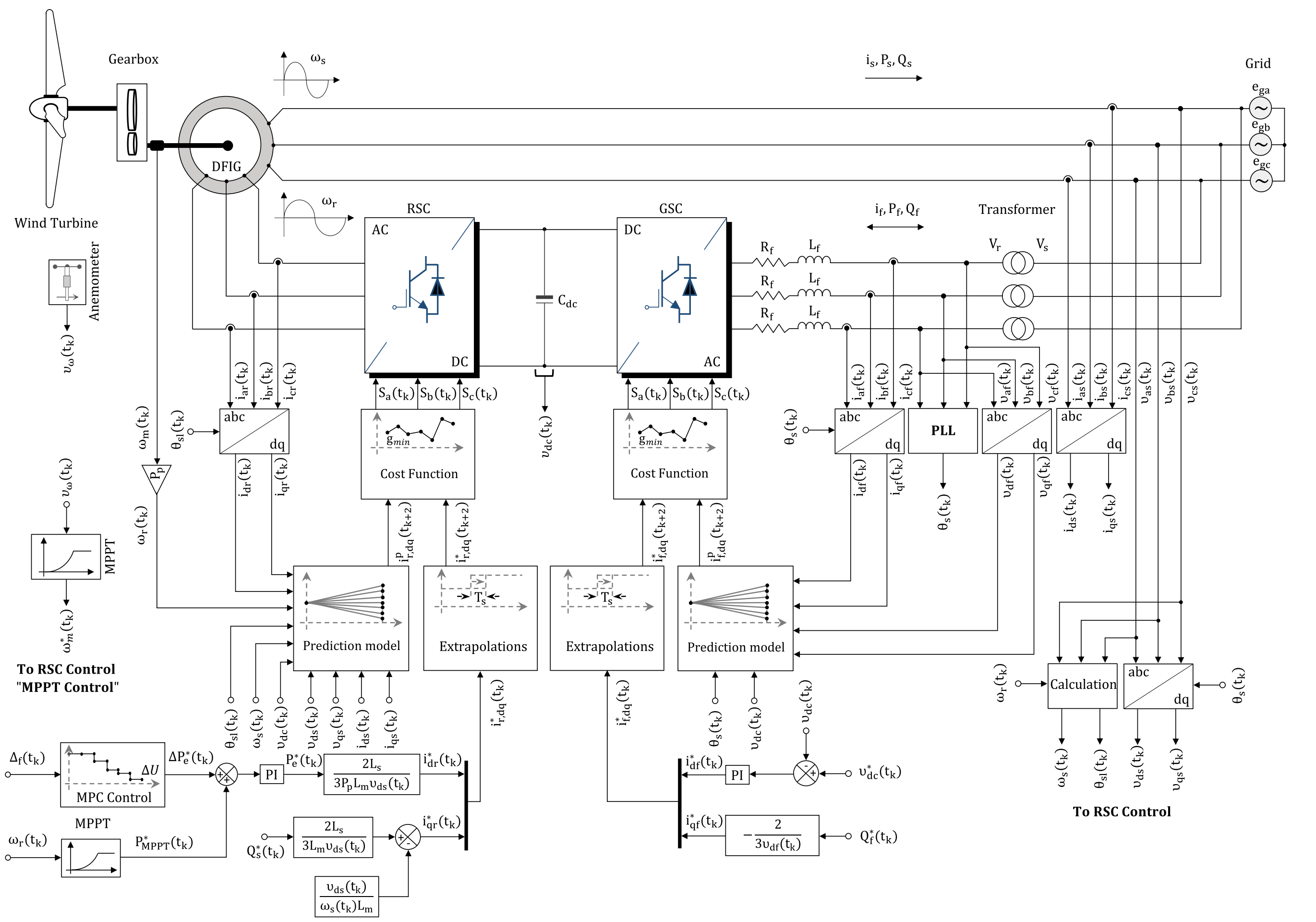

Figure 5. DFIG-based WT overall control scheme.

3.4. Continuous Control Set-Model Predictive Control (CCS-MPC) for DFIG-Based Wind Turbine Participation in Frequency Support

Currently, the WTS′ inertial response is obtained by introducing an additional power control loop. During frequency events, this loop increases the WT output power to meet power imbalance. The traditional controller consists of two separate loops, an artificial inertial loop, proposed in [44], its output control signal is proportional to the frequency derivative. The second loop is a droop-based characteristic, its control sets are proportional to the frequency deviation [45]. The control scheme is shown in Figure 6 [46]. K_{in} is a coefficient that scales the frequency derivative, whereas K_D scales the frequency deviation. A high-pass filter on the droop loop is used in order to eliminate continuous activation of the control system by permanent frequency deviation and transient variations. Thus, a low-pass filter is placed on the frequency differentiator loop with the aim of ensuring that the frequency measurement noise does not affect the system. The requested power is regulated by the rotor side converter (RSC) controller by adjusting the rotor current $i_r^d(t_k)$. It is supplied as a deceleration kinetic energy. In this way, the WT emulates the behavior of the traditional synchronous generator and virtually reinforce the total power system inertia.

In order to overcome all the mentioned limitations, the MPC uses the power system dynamics shown by Equation (21). The frequency deviation represents the frequency controller input, while the additional active power reference is its output. The model of frequency response illustrated in Figure 7 is composed of an active power response unit based on MPC which is added to a rotor speed response unit according to traditional MPPT.

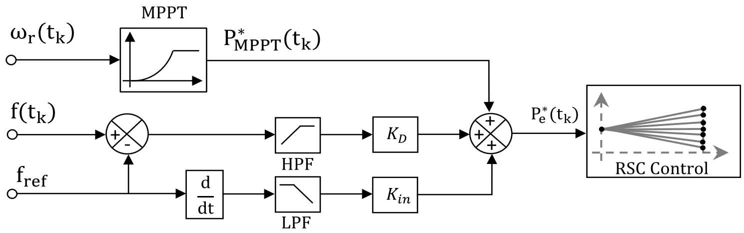

Figure 6. Inertial controller. Upper section: MPPT control. Middle section: frequency droop control. Lower section: inertia emulation.

$$\begin{cases} \Delta f(t_{k+1}) = -\frac{\mathbf{D}}{\mathbf{2H}}\Delta f(t_k) + \frac{\mathbf{1}}{\mathbf{2H}}\Delta P_e(t_k) \\ 0 < \Delta P_e(t_k) \leq P_{OPPT} - P_{MPPT} \end{cases} \tag{21}$$

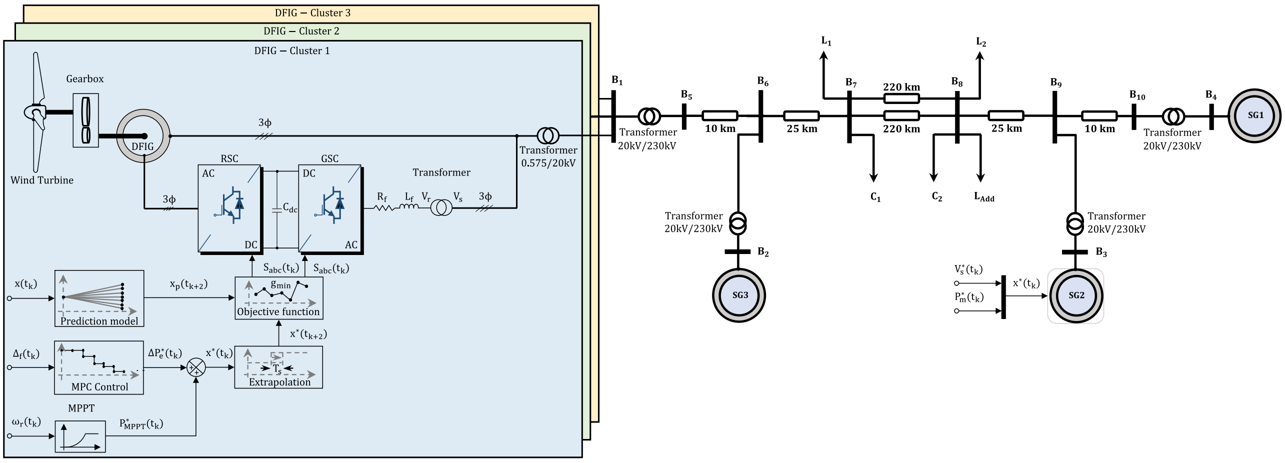

Figure 7. Kundur's AC grid simulation system.

The power system dynamic model is a sole input and a sole output, according to Equation (22) [47].

$$\begin{cases} x_m(t_{k+1}) = \mathbf{A_m} x_m(t_k) + \mathbf{B_m} u(t_k) \\ y(t_k) = \mathbf{C_m} x_m(t_k) + \mathbf{D_m} u(t_k) \end{cases} \tag{22}$$

where $u(t_k)$ is the control variable, $y(t_k)$ is the system output, and $x_m(t_k)$ is the state variable.

Subtracting both sides of Equation (22) leads to;

$$\begin{aligned} x_m(t_{k+1}) - x_m(t_k) = {} & \mathbf{A_m}(x_m(t_k) - x_m(t_{k-1})) \\ & + \mathbf{B_m}(u(t_k) - u(t_{k-1})) \end{aligned} \tag{23}$$

The state and control variable differences are designated by

$$\begin{cases} \Delta x_m(t_{k+1}) = x_m(t_{k+1}) - x_m(t_k); \\ \Delta x_m(t_k) = x_m(t_k) - x_m(t_{k-1}); \\ u(t_k) = u(t_k) - u(t_{k-1}) \end{cases} \tag{24}$$

The state space model receives as input $\Delta u(t_k)$. In order to attach $\Delta x_m(t_k)$ to the output $y(t_k)$, a new vector containing state variables is defined as $x(t_k) = \begin{bmatrix} \Delta x_m(t_k)^T & y(t_k) \end{bmatrix}^T$

$$\begin{aligned} y(t_{k+1}) - y(t_k) &= \mathbf{C_m}(x_m(t_k) - x_m(t_{k-1})) \\ &= \mathbf{C_m}\Delta x_m(t_{k+1}) \\ &= \mathbf{C_m}\mathbf{A_m}\Delta x_m(t_k) + \mathbf{C_m}\mathbf{B_m}\Delta u(t_k) \end{aligned} \tag{25}$$

This induces a new state space model, described in Equation (26).

$$\begin{cases} \overbrace{\begin{bmatrix} \Delta x_m(t_{k+1}) \\ y(t_{k+1}) \end{bmatrix}}^{x(t_{k+1})} & = \overbrace{\begin{bmatrix} \mathbf{A_m} & o_m^T \\ \mathbf{C_m A_m} & \mathbf{C_m B_m} \end{bmatrix}}^{\mathbf{A}} \cdot \overbrace{\begin{bmatrix} \Delta x_m(t_k) \\ y(t_k) \end{bmatrix}}^{x(t_k)} \\ & + \overbrace{\begin{bmatrix} \mathbf{B_m} \\ \mathbf{C_m B_m} \end{bmatrix}}^{\mathbf{B}} \cdot \Delta u(t_k) \\ y(t_k) & = \overbrace{\begin{bmatrix} o_m & 1 \end{bmatrix}}^{\mathbf{C}} \cdot \begin{bmatrix} \Delta x_m(t_k) \\ y(t_k) \end{bmatrix} \end{cases} \tag{26}$$

where, $o_m = \overbrace{\begin{bmatrix} 0 & 0 & . & . & . & 0 \end{bmatrix}}^{n}$, n represents the state vector size. The augmented model (**A**, **B**, **C**) is formulated based on the system parameters. At sampling time $k_i, k_i > 0$ the state variable $x(t_{k_i})$ is directly measured, the current frequency information is provided by the state variable $x(t_{k_i})$. The future control trajectory is denoted by

$$\Delta u(t_{k_i}), \Delta u(t_{k_i+1}), \Delta u(t_{k_i+2}), \ldots, \Delta u(t_{k_i+N_c-1})$$

where N_C denotes the control horizon, and using the available $x(t_{k_i})$, the state variables are predicted for a prediction horizon of N_P. N_P denotes the length of the optimization window. The incoming state variables are denoted by

$$x(t_{k_i+1}|t_{k_i}), x(t_{k_i+2}|t_{k_i}), \ldots, x(t_{k_i+m}|t_{k_i}), \ldots, x(t_{k_i+N_p}|t_{k_i})$$

where $x(t_{k_i+m}|t_{k_i})$ corresponds to the predicted state variable at t_{k_i+m} with the available $x(t_{k_i})$ information. Based on (**A**, **B**, **C**) the future control parameters and predicted states, the incoming state variables are computed sequentially in a stepwise manner.

$$\begin{cases} x(t_{k_i+1}|t_{k_i}) & = \mathbf{A}x(t_{k_i}) + \mathbf{B}\Delta u(t_{k_i}) \\ x(t_{k_i+2}|t_{k_i}) & = \mathbf{A}x(t_{k_i+1}|t_{k_i}) + \mathbf{B}\Delta u(t_{k_i+1}) \\ & . \\ & . \\ & . \\ x(t_{k_i+N_P}|t_{k_i}) & = \mathbf{A^{N_P}}x(t_{k_i}) + \mathbf{A^{N_P-1}B}\Delta u(t_{k_i}) \\ & + \mathbf{A^{N_P-2}B}\Delta u(t_{k_i+1}) + \mathbf{B}\Delta u(t_{k_i+1}) +, \ldots, \\ & + \mathbf{A^{N_P-N_C}B}\Delta u(t_{k_i+N_C-1}) \end{cases} \tag{27}$$

$$\begin{cases} y(t_{k_i+1}|t_{k_i}) & = \mathbf{CA}x(t_{k_i}) + \mathbf{CB}\Delta u(t_{k_i}) \\ y(t_{k_i+2}|t_{k_i}) & = \mathbf{CA^2}x(t_{k_i}) + \mathbf{CAB}\Delta u(t_{k_i}) \\ & + \mathbf{CB}\Delta u(t_{k_i+1}) \\ y(t_{k_i+3}|t_{k_i}) & = \mathbf{CA^3}x(t_{k_i}) + \mathbf{CA^2B}\Delta u(t_{k_i}) \\ & + \mathbf{CAB}\Delta u(t_{k_i+1}) + \mathbf{CB}\Delta u(t_{k_i+1}) \\ & . \\ & . \\ & . \\ y(t_{k_i+N_P}|t_{k_i}) & = \mathbf{CA^{N_P}}x(t_{k_i}) + \mathbf{CA^{N_P-1}B}\Delta u(t_{k_i}) \\ & + \mathbf{CA^{N_P-2}B}\Delta u(t_{k_i+1}) + \mathbf{B}\Delta u(t_{k_i+1}) +, \ldots, \\ & + \mathbf{CA^{N_P-N_C}B}\Delta u(t_{k_i+N_C-1}) \end{cases} \tag{28}$$

$x(t_{k_i+m})$ are formulated as information based on $x(t_{k_i})$ and $\Delta u(t_{k_i+j})$, where $j = 0, 1, \ldots N_C - 1$. Y and ΔU are defined as follows

$$Y = \left[y(t_{k_i+1}|t_{k_i}), y(t_{k_i+2}|t_{k_i}), \ldots, y(t_{k_i+N_P}|t_{k_i})\right]^T \tag{29}$$
$$\Delta U = \left[\Delta u(t_{k_i+1}|t_{k_i}), \Delta u(t_{k_i+2}|t_{k_i}), \ldots, \Delta u(t_{k_i+N_P}|t_{k_i})\right]^T$$

Y and ΔU are N_P and N_C dimension. The final compact matrix form of the state model is

$$Y = \mathbf{F}x(t_{k_i}) + \boldsymbol{\phi}\Delta U \tag{30}$$

where;

$$\mathbf{F} = \begin{bmatrix} \mathbf{CA} \\ \mathbf{CA^2} \\ \mathbf{CA^3} \\ . \\ . \\ . \\ \mathbf{CA^{N_P}} \end{bmatrix} \tag{31}$$
$$\boldsymbol{\phi} = \begin{bmatrix} \mathbf{CB} & 0 & \ldots & 0 \\ \mathbf{CAB} & \mathbf{CB} & \ldots & 0 \\ \mathbf{CA^2B} & \mathbf{CAB} & \ldots & 0 \\ \vdots & \vdots & \ddots & \vdots \\ \mathbf{CA^{N_P-1}B} & \mathbf{CA^{N_P-2}B} & \ldots & \mathbf{CA^{N_P-N_C}B} \end{bmatrix}$$

At t_{k_i} and a given reference $r(t_{k_i})$, the MPC reduces the discrepancy between the predicted output and the reference. This is achieved by selecting the best ΔU control vector that minimizes the error function. The data vector containing the setpoint is

$$R_s^T = \overbrace{\begin{bmatrix} 1 & 1 & . & . & . & 1 \end{bmatrix}}^{N_P} r(t_{k_i}) = \bar{\boldsymbol{R}} r(t_{k_i})$$

The controller cost function J is defined by Equation (32).

$$J = (R_s - Y)^T(R_s - Y) + \Delta U^T \bar{\boldsymbol{R}} \Delta U \tag{32}$$

The first term consists of the squared error minimization, the significance of the value of ΔU is captured by the second term. $\bar{\boldsymbol{R}}$ is a diagonal matrix as $\bar{\boldsymbol{R}} = r_\omega I_{N_C x N_C}$.

where r_ω represents the optimization parameter. It ensures the desired closed loop performance. If $r_\omega = 0$, the controller does not pay special attention to the output value of ΔU and only takes care of minimizing the error $(R_s - Y)^T(R_s - Y)$. In the case of a large r_ω, the ΔU values are smaller. To find the optimal ΔU that minimizes J, using Equation (30), J becomes

$$J = (R_s - \boldsymbol{F}x(t_{k_i}))^T(R_s - \boldsymbol{F}x(t_{k_i})) - 2\Delta U^T \boldsymbol{\phi}^T$$
$$(R_s - \boldsymbol{F}x(t_{k_i}))\bar{\boldsymbol{R}}\Delta U + \Delta U^T(\boldsymbol{\phi}^T\boldsymbol{\phi} + \bar{\boldsymbol{R}})\Delta U \tag{33}$$

The optimal solution for the control signal expressed by Equation (35) is obtained at the point where $\frac{\partial J}{\partial \Delta U} = 0$.

$$\frac{\partial J}{\partial \Delta U} = -2\boldsymbol{\phi}^T(R_s - \boldsymbol{F}x(t_{k_i})) + 2(\boldsymbol{\phi}^T\boldsymbol{\phi} + \bar{\boldsymbol{R}})\Delta U = 0 \tag{34}$$

$$\Delta U = (\boldsymbol{\phi}^T\boldsymbol{\phi} + \bar{\boldsymbol{R}})^{-1}\boldsymbol{\phi}^T(R_s - \boldsymbol{F}x(t_{k_i})) \tag{35}$$

With the existence and uniqueness of the Hessian matrix $(\boldsymbol{\phi}^T\boldsymbol{\phi} + \bar{\boldsymbol{R}})^{-1}$, the control signal can be calculated. Its optimal solution is related to the reference signal $r(tk_i)$ and the state variable $x(t_{k_i})$ as follows

$$\Delta U = (\boldsymbol{\phi}^T\boldsymbol{\phi} + \bar{\boldsymbol{R}})^{-1}\boldsymbol{\phi}^T(\bar{\boldsymbol{R}}r(t_{k_i}) - \boldsymbol{F}x(t_{k_i})) \tag{36}$$

Algorithm 2 illustrates the proposed control scheme for frequency support.

Since we are dealing with a controller that will have to equip each WT, the number of clusters formulating the wind farm are not affecting the performance of the proposed controller. However, the computational time is strongly impacted by the parameters N_p and N_c determining the control horizon chosen by the user.

Algorithm 2 CCS-MPC Frequency Control Algorithm.

SET $(\boldsymbol{A_m}, \boldsymbol{B_m}, \boldsymbol{C_m}, \boldsymbol{N_P}, \boldsymbol{N_C})$ and MEASURE $(\mathbf{r}(\mathbf{t_{k_i}}))$
FORMULATION $(\boldsymbol{F}, \boldsymbol{\phi}, \boldsymbol{R_s})$
    for i = 1,. . . ,N_P

$$\boldsymbol{R_s} \leftarrow \overbrace{\begin{bmatrix} 1 & 1 & . & . & . & 1 \end{bmatrix}}^{N_P} r(t_{k_i})$$

        for j = 1,. . . ,N_C
        $(\boldsymbol{F}, \boldsymbol{\phi}) \leftarrow$ **Equation** (31).
        end
    end
MINIMIZATION $(\boldsymbol{J})$

$$\mathbf{\Delta U} \leftarrow (\boldsymbol{\phi}^T\boldsymbol{\phi} + \bar{\boldsymbol{R}})^{-1}\boldsymbol{\phi}^T(\bar{\boldsymbol{R}}r(t_{k_i}) - \boldsymbol{F}x(t_{k_i}))\ \textbf{Equation}(36).$$

$$\mathbf{\Delta U}(\mathbf{t_{k_i}}) \leftarrow \overbrace{\begin{bmatrix} 1 & 0 & . & . & . & 0 \end{bmatrix}}^{N_C} \Delta U.$$

RETURN $\mathbf{U}(\mathbf{t_{k_i}}) \leftarrow \mathbf{\Delta U}(\mathbf{t_{k_i}}) + \mathbf{U}(\mathbf{t_{k_i-1}})$.

4. Case Studies

The Kundur′s two-areas power grid model illustrated in Figure 7 [48] is used to demonstrate the effectiveness of the proposed MPC-based frequency control strategy. Ref. [48] details the synchronous generators (SGs) and automatic voltage regulators (AVRs) parameters. Furthermore, Figure 8 and Table 2 highlight the steam turbine governor model and its relevant constants, respectively [48,49]. SGs use the Type PSS4C multi-band power system stabilizer with the detailed model and parameters in [50]. Parameters of the synchronous generators and loads are illustrated in Tables A1 and A2.

The DFIG-based WTS parameters are illustrated in Table A3. The WF consists of three aggregated clusters consisting of 100 DFIG-based WTs of 1.5 MW each. A 20/230 kV − 900 MVA transformer station and a 10 km long 230 kV transmission line connect the WF to the power grid.

Figure 1 shows the WT power characteristics, its input wind speed is 6 m/s, its rated speed is 12 m/s, the operating window of the DFIG rotor speed is between 0.7 p.u and 1.2 p.u.

Nevertheless, it is reminded that the contribution of this paper aims only at primary frequency control, no secondary frequency control means have been designed for SGs.

The performance of the proposed controller was evaluated under different wind with load variation conditions. The frequency controller was tested over the entire operating band of the DFIG to determine its stability. Three cases summarize this: operation with wind speed of 8 m/s at Cluster 1, 9 m/s at Cluster 2, 11 m/s, at Cluster 3 and 160 MW overload in the power grid. Furthermore, the controller was also tested during permanent wind variations. The efficiency of the proposed MPC controller is compared with the generic combined inertial and droop control, in which R is set to 5% [26], and K_{in} is set to $2 * H$ [1]. In addition, it is compared with the sectional droop controller, in which the droop is dynamically adjusted according to Figure 9.

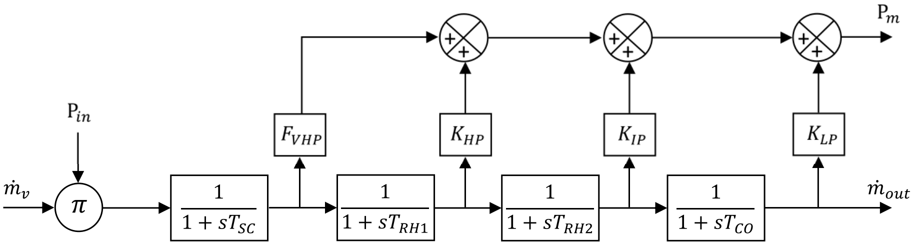

Figure 8. IEEE-G tandem compound steam turbine governor model.

Table 2. Parameters of The IEEE-G tandem compound steam turbine governor model.

K_{VHP}	K_{HP}	K_{IP}	K_{LP}
0	0.36	0.36	0.28
T_{SC} (s)	T_{RH1} (s)	T_{RH2} (s)	T_{CO} (s)
0.5	3.3	10	1

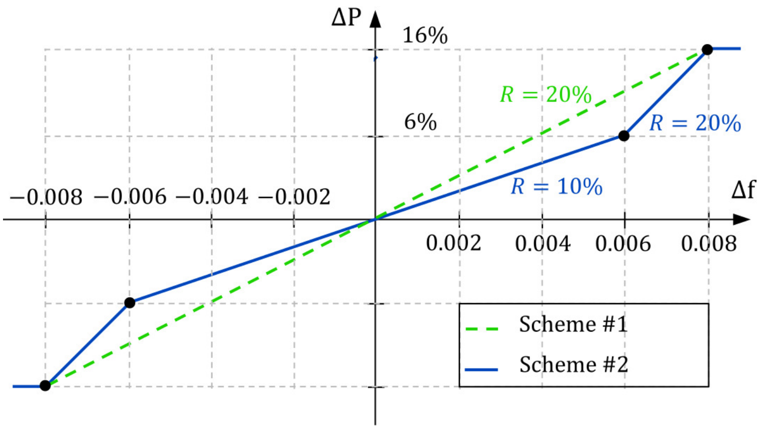

Figure 9. Conventional and sectional droop control. Scheme #1 [26] and Scheme #2 [28].

4.1. Case 1: Wind Speed of 8 m/s at Cluster 1, 9 m/s at Cluster 2, 11 m/s at Cluster 3 and 160 MW Overload in the Power Grid

Figures 10 and 11 outline the obtained results during the simulation of case study 1.

Figure 10a show that with the proposed control scheme, the FN is arrested closely to the settling frequency, the obtained FN for MPPT operation, scheme #1, scheme #2, and the proposed scheme are evaluated to 49.8503, 49.8401, 49.8367, and 49.8324 Hz, respectively. Δf is increased from −0.1676 to −0.1497 Hz as depicted in Figure 10b. The overproduction ensured by scheme #1, scheme #2 are almost the same during the initial stage, the overproduction is ensured for about 40s, then decreases rapidly with the frequency settling until reaching a much lower level and leave for the SGs that take over the excess demand. However, in the proposed controller, the overproduction slowly increases to reach its maximum level after about 8s, then slowly decreases and causes a deceleration of the DFIG-Based WTS, which restores more kinetic energy compared to conventional schemes.

In scheme #1 and scheme #2, the rapid cancellation of overproduction lead to the rotor speed recovery process to the MPPT points (Figures 10d and 11a), which are ω_r = 0.8 p.u in Cluster 1, ω_r = 0.9 p.u in Cluster 2, and ω_r = 1.1 p.u in Cluster 3. In the proposed scheme, this recovery is not allocated, the rotor speed converges to ω_r = 0.7088 p.u in Cluster 1, ω_r = 0.7539 p.u in Cluster 2, ω_r = 0.9690 p.u in Cluster 3, and stabilizes at these points until the frequency is restored to its nominal band during the secondary control. It is this deceleration that allowed us to restore enough kinetic energy to the power grid and arrest the FN at the value closest to settling frequency which amounts to 49.8761 Hz. It can also be observed in Figure 10a,b that, with the proposed scheme, no oscillations were experienced in the power system frequency and the WTs output power. While with scheme #1 and scheme #2, the output power and frequency have remarkable oscillations and take longer to achieve the new steady state.

Figure 10b also illustrates that the WT rotor speed does not oscillate, which means the alleviation of mechanical stresses exerted on the WTs′ shafts. This is significantly important for power systems experiencing high WFs penetration with very large capacities. Figure 11a,b show that the stabilized operation point under the proposed controller is slightly lower than that of MPPT operation, as with the proposed controller, the WTs continue to operate at the OPPT point. However, the settling frequency difference between the two points is only 0.0064 Hz, which is very minimal. Meanwhile, the settling time for reaching the new frequency steady state is significantly improved by 10.51 s by the proposed controller compared to the conventional control, the settling time of scheme #1 and scheme #2 and the proposed scheme are evaluated to 43.5954, 42.3113, and 31.7937 s, respectively. Obtained results are summarized in Table 3 and Figure 11c,d.

Table 3. Obtained results for case 1.

Parameter	**Controller**		**Results**
Frequency Nadir (Hz)	Proposed		49.8503
	Scheme #2		49.8401
	Scheme #1		49.8367
	MPPT		49.8324
Maximum frequency deviation (Hz)	Proposed		−0.1497
	Scheme #2		−0.1599
	Scheme #1		−0.1633
	MPPT		−0.1676
Settling time (s)	Proposed		31.7937
	Scheme #2		42.3113
	Scheme #1		43.5954
Settling frequency (Hz)	Proposed		49.8761
	Scheme #2		49.8836
	Scheme #1		49.8836
	MPPT		49.8831
Converged rotor speed (p.u)	Proposed	Cluster 1	0.7088
		Cluster 2	0.7539
		Cluster 3	0.9690
	Scheme #1 & #2	Cluster 1	0.8001
		Cluster 2	0.9002
		Cluster 3	1.1002

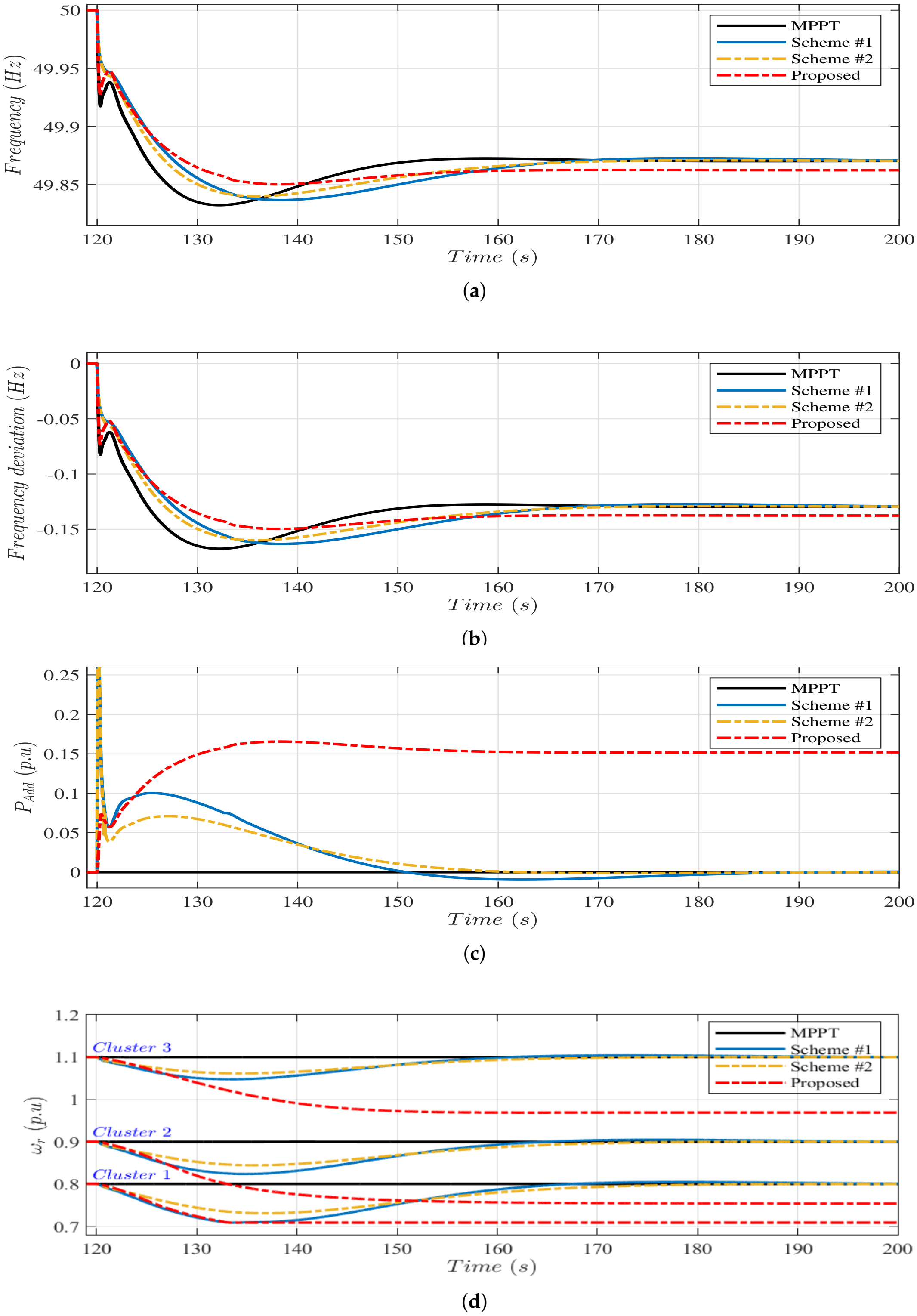

Figure 10. Simulation results for case 1. (**a**) Frequency. (**b**) Frequency deviation. (**c**) Additional power. (**d**) Rotor speed.

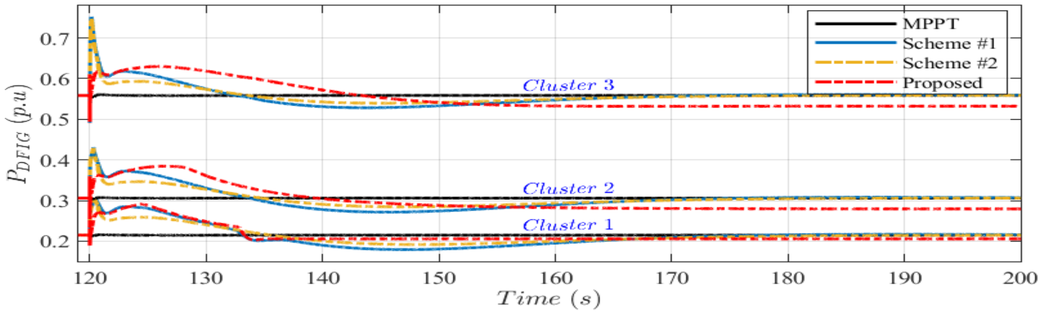

(**a**)

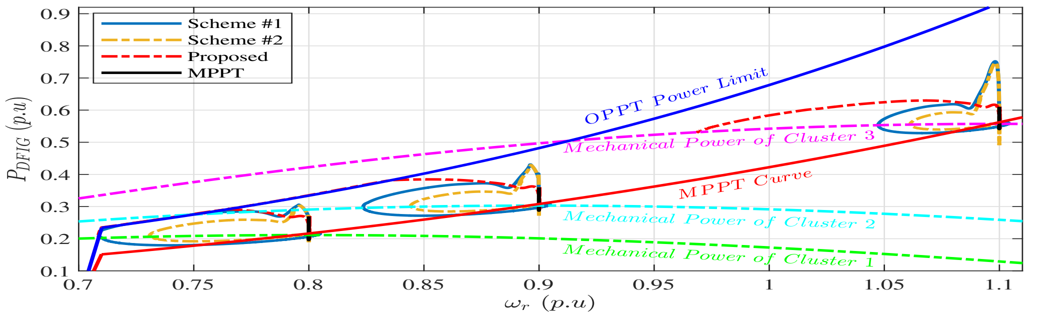

(**b**)

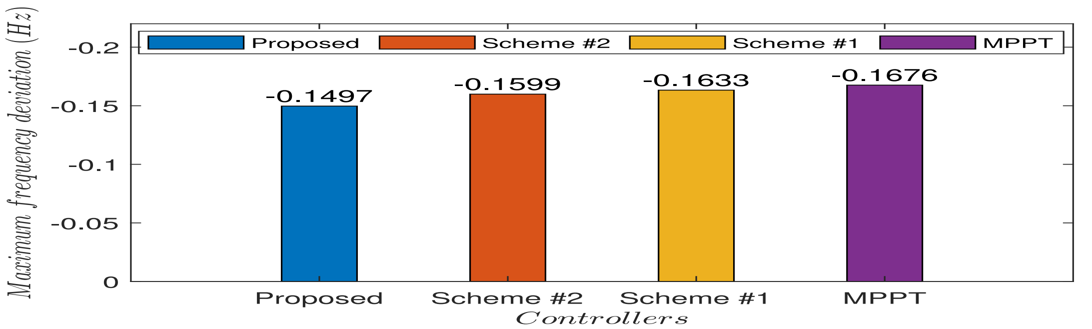

(**c**)

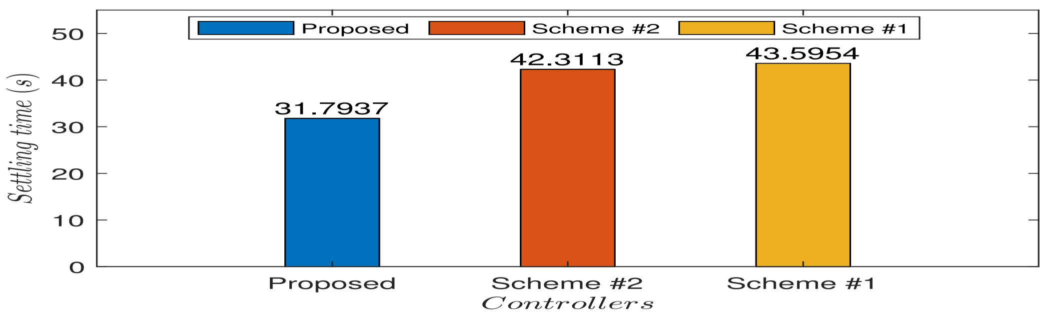

(**d**)

Figure 11. Simulation results for case 1. (**a**) WTS power. (**b**) WTS power–speed trajectory. (**c**) Comparison results for frequency deviation. (**d**) Comparison results for settling time.

4.2. Case 2: Variable Wind Speeds and Fixed Load

The obtained results during the simulation of case study 2 are shown in Figure 12.

Remarkable fluctuations are caused by changes in weather conditions, especially wind speed. In order to evaluate the robustness to these data, a variation of ± 0.5 m/s was introduced in the different sites as shown in Figure 12a. It can be observed that the proposed MPC predictive controller damped the oscillation of the system frequency considerably compared to the traditional controllers. This is due to the fact that the output of the MPC controller is optimally calculated following the actual deviation caused by the change in wind speed while the traditional controllers rely on well-defined droop and coefficients beforehand. Furthermore, the results show that traditional controllers have more irregular frequency responses. The performance of the different controllers was evaluated using a set of performance indicators as expressed by Equation (37) [51].

Obtained results are shown in the Figure 12 and Table 4.

$$\begin{cases} ISE = \int_0^{\infty} (f - f_{nom})^2 \mathrm{d}t \\ ITSE = \int_0^{\infty} t \cdot (f - f_{nom})^2 \mathrm{d}t \\ IAE = \int_0^{\infty} |(f - f_{nom})| \mathrm{d}t \\ ITAE = \int_0^{\infty} t \cdot |(f - f_{nom})| \mathrm{d}t \end{cases} \tag{37}$$

Table 4. Comparison of performance index for case 2.

Control Scheme	ISE	ITSE	IAE	ITAE
Proposed	0.0028	0.0202	0.3022	6.7177
Scheme #1	0.0069	0.0502	0.4180	8.1983
Scheme #2	0.0070	0.0542	0.4322	8.2305
MPPT operation	0.0095	0.0567	0.4531	9.2788

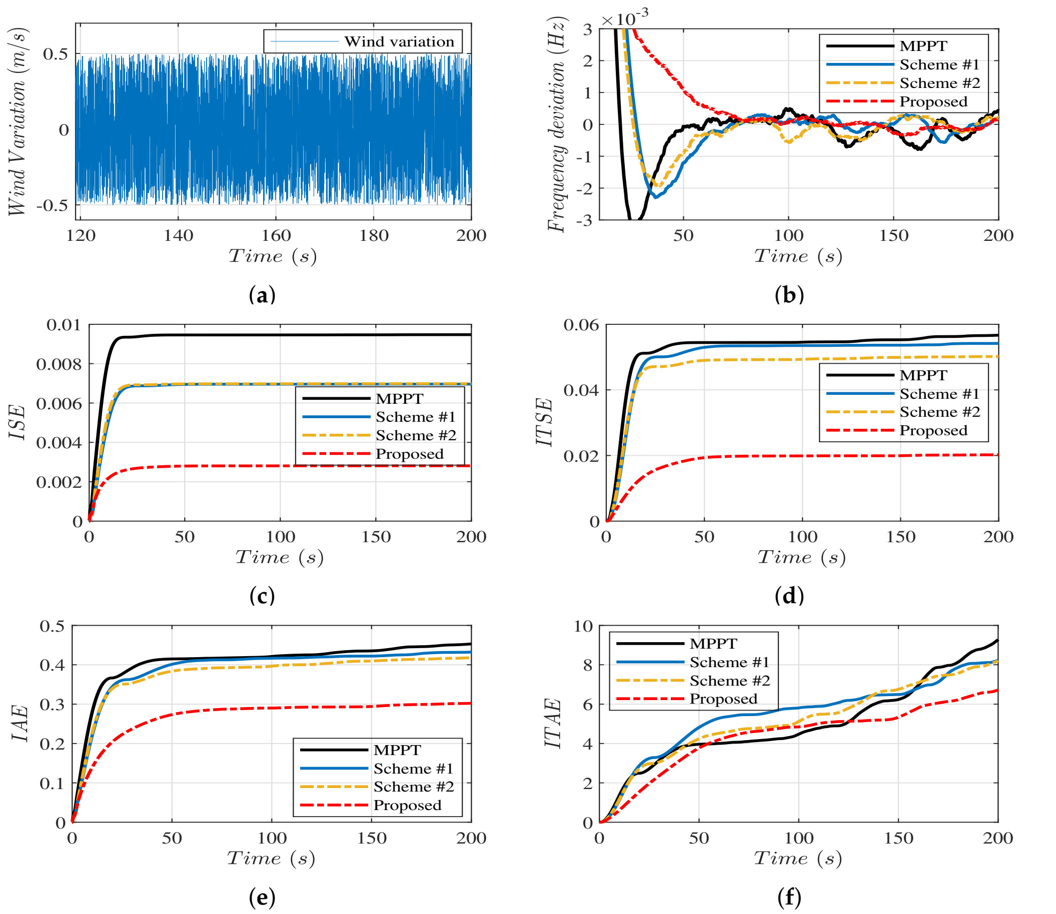

Figure 12. Simulation results for case 2. (**a**) Wind variation. (**b**) Frequency. (**c**) ISE. (**d**) ITSE. (**e**) IAE. (**f**) ITAE.

5. Conclusions

This paper proposes a fast MPC-based frequency support controller using the the WTs rotational stored kinetic energy in multi-clusters wind farm. The suggested scheme raises the FN closely to the settling frequency, which reduces the mechanical stresses on the WTs during frequency events. The key novelties of the proposed scheme are listed as follows:

- The frequency Nadir enhancement: The FN is arrested closely to the settling frequency. Indeed, the FN is improved by more than 6.1% compared to conventional schemes.
- Eliminating SFDs through the WTS's rotor speed recovery approach: WTS rotor speed is not designed to revert back to the MPPT point during the main frequency support. This means that the WT does not consume any additional power from the grid for speed recovery to MPPT during the frequency event. Therefore, no SDF will occur.
- Improving the frequency settling time: the fast MPC-based controller has enhanced the settling time for reaching the new frequency steady state by more than 10.51 s, compared to conventional schemes.
- Improving the frequency response during transient wind conditions and fluctuations.

Regarding the difference in wind conditions between sites on controller performance, the stability of the WTs is ensured for all the operating band.

Author Contributions: Conceptualization, Y.A.A. and M.O.; methodology, Y.A.A. and M.O.; software, Y.A.A.; validation, Y.A.A., M.O., S.-H.L. and Z.C.; formal analysis, Y.A.A. and Z.C.; investigation, S.-H.L. and Z.C.; resources, M.O., Z.C. and S.-H.L.; writing—original draft preparation, Y.A.A. and M.O.; writing—review and editing, Y.A.A., M.O., Z.C. and S.-H.L.; supervision, M.O.; project administration, M.O.; funding acquisition S.-H.L. All authors have read and agreed to the published version of the manuscript.

Funding: This work was partly supported by the Research Centre for Engineering in Smart and Sustainable Systems of Mohammed V University in Rabat, Morocco. It is was also supported by the Korea Institute of Energy Technology Evaluation and Planning (KETEP) Grant funded by the Korea Government (MOTIE) in part (Development of DC Power Trade Platform System in Public Community Which is Connected by EV-Renewable Based on Block Chain Technology) under Grant 20192010107050, and in part (20223A10100030, Development of Synchronous Condenser Model and Power System Inertia Operating Technology).

Data Availability Statement: The data used in this research are available in the paper.

Conflicts of Interest: The authors declare no conflict of interest.

Abbreviations

The following abbreviations are used in this manuscript:

CCS-MPC	Continuous Control Set Model Predictive Control.
DFIG	Doubly-Fed Induction Generator.
FCS-MPC	Finite Control Set Model Predictive Control.
FN	Frequency Nadir.
GSC	Grid Side Converter.
IGBT	Insulated-Gate Bipolar Transistor.
MPPT	Maximum Power Point Tracking.
OPPT	Optimal Power Point Tracking.
PSO	Power System Operator.
ROCOF	Rate Of Change Of Frequency.
RSC	Rotor Side Converter.
SFD	Second Frequency Dip.
WF	Wind Farm.
WT	Wind Turbine.
f, f_{nom}	Actual and nominal system frequency.
Δf	Frequency deviation.
df/dt	Frequency derivative.

P_m	WT mechanical output power.
v_ω	WT input Wind speed.
β	Pitch angle.
ω_r	DFIG rotor speed.
ω_{rmin}	Cut-in rotor speed.
ω_{rmax}	Rated rotor speed.
K_{Opt}	Optimal coefficient for MPPT control.
$K_{in},\ K_D$	ROCOF and droop loop gains.
H	WT inertia constant.
v_s^k, i_s^k	dq-axis stator voltage and current components.
v_r^k, i_r^k	dq-axis rotor voltage and current components.
v_f^k, i_f^k	dq-axis filter voltage and current components.
t_k	Current sampling time.

Appendix A

Table A1. Operating parameters of synchronous generator.

Parameter	Value
Rated Power P_e (MVA)	900.00
D-Axis Synchronous Reactance X_d (p.u)	1.8000
Q-Axis Synchronous Reactance X_q (p.u)	1.7000
Stator Resistance R_a (p.u)	0.0025
Stator Leakage Inductance X_l (p.u)	0.2000
D-Axis Transient Reactance $X_d^{'}$ (p.u)	0.3000
Q-Axis Transient Reactance $X_q^{'}$ (p.u)	0.5500
D-Axis Subtransient Reactance $X_d^{''}$ (p.u)	0.2500
Q-Axis Subtransient Reactance $X_q^{''}$ (p.u)	0.2500
D-Axis Transient Open Circuit Time Constant $T_{d0}^{'}$ (s)	8.0000
Q-Axis Transient Open Circuit Time Constant $T_{q0}^{'}$ (s)	0.4000
D-Axis Subtransient Open Circuit Time Constant $T_{d0}^{''}$ (s)	0.0300
Q-Axis Subtransient Open Circuit Time Constant $T_{q0}^{''}$ (s)	0.0500
Total inertia constant H (s)	6.5000

Appendix B

Table A2. Loads and shunt capacitance connected in Kundur's AC grid.

Bus	Load	Shunt Capacitance
Bus B_7	$(900 + j100)$ MVA	200 MVAr
Bus B_8	$(900 + j100)$ MVA	350 MVAr

Appendix C

Table A3. Parameters of DFIG-based WTS.

Parameter	Value
Rated Power P_e (MVA)	1.50000
Rated Stator Voltage v_s (V)	575.000
Rated Frequency f (Hz)	50.0000
Stator Resistance R_s (p.u)	0.00706
Rotor Resistance R_r (p.u)	0.00500
Stator Inductance L_s (p.u)	0.17100
Rotor Inductance L_r (p.u)	0.15600
Mutual Inductance L_m (p.u)	2.90000
Pole Pairs p	3

Table A3. *Cont.*

Parameter	Value
Leakage constant σ (p.u)	$1-\frac{L_m^2}{L_s L_r}$
Converters rated power (p.u)	0.5
Total inertia constant H (s)	5.04000
ω_{rmin} (p.u)	0.70000
ω_{rmax} (p.u)	1.20000
$[\beta^{\circ}_{min}, \beta^{\circ}_{max}]$	[0.00000, 45.0000]
Maximum $\frac{d\beta}{dt}$ $(^{\circ}/s)$	2.00000
$[c_1, c_2, c_3, c_4, c_5, c_6]$	[0.5176, 116, 0.4, 5, 21, 0.0068]
v_{nom} (m/s) at $P_e = 0.73$ (p.u)	12.0000
K_{Opt}	0.42250
K_{in}	$2H$
K_D	$\frac{1}{R(\%)}$
Pitch controller gain K_p	500

References

1. Yingcheng, X.; Nengling, T. System frequency regulation in doubly fed induction generators. *Int. J. Electr. Power Energy Syst.* **2012**, *43*, 977–983. [CrossRef]
2. Datta, U.; Shi, J.; Kalam, A. Primary frequency control of a microgrid with integrated dynamic sectional droop and fuzzy based pitch angle control. *Int. J. Electr. Power Energy Syst.* **2019**, *111*, 248–259. [CrossRef]
3. Tian, X.; Wang, W.; Chi, Y.; Li, Y.; Liu, C. Virtual inertia optimisation control of DFIG and assessment of equivalent inertia time constant of power grid. *IET Renew. Power Gener.* **2018**, *12*, 1733–1740. [CrossRef]
4. Zhang, Y.; Melin, A.M.; Djouadi, S.M.; Olama, M.M.; Tomsovic, K. Provision for Guaranteed Inertial Response in Diesel-Wind Systems via Model Reference Control. *IEEE Trans. Power Syst.* **2018**, *33*, 6557–6568. [CrossRef]
5. Liu, F.; Liu, Z.; Mei, S.; Wei, W.; Yao, Y. ESO-Based Inertia Emulation and Rotor Speed Recovery Control for DFIGs. *IEEE Trans. Energy Convers.* **2017**, *32*, 1209–1219. [CrossRef]
6. Van de Vyver, J.; De Kooning, J.D.M.; Meersman, B.; Vandevelde, L.; Vandoorn, T.L. Droop Control as an Alternative Inertial Response Strategy for the Synthetic Inertia on Wind Turbines. *IEEE Trans. Power Syst.* **2016**, *31*, 1129–1138. [CrossRef]
7. Tan, Y.; Meegahapola, L.; Muttaqi, K.M. A Suboptimal Power-Point-Tracking-Based Primary Frequency Response Strategy for DFIGs in Hybrid Remote Area Power Supply Systems. *IEEE Trans. Energy Convers.* **2016**, *31*, 93–105. [CrossRef]
8. Wang, Z.; Wu, W. Coordinated Control Method for DFIG-Based Wind Farm to Provide Primary Frequency Regulation Service. *IEEE Trans. Power Syst.* **2018**, *33*, 2644–2659. [CrossRef]
9. Ghosh, S.; Kamalasadan, S.; Senroy, N.; Enslin, J. Doubly Fed Induction Generator (DFIG)-Based Wind Farm Control Framework for Primary Frequency and Inertial Response Application. *IEEE Trans. Power Syst.* **2016**, *31*, 1861–1871. [CrossRef]
10. Wang, S.; Hu, J.; Wang, S.; Tang, H.; Chi, Y. Comparative study on primary frequency control schemes for variable-speed wind turbines. *J. Eng.* **2017**, *2017*, 1332–1337. [CrossRef]
11. Zhang, X.; Zha, X.; Yue, S.; Chen, Y. A Frequency Regulation Strategy for Wind Power Based on Limited Over-Speed De-Loading Curve Partitioning. *IEEE Access* **2018**, *6*, 22938–22951. [CrossRef]
12. Gomez, L.A.G.; Lourenco, L.F.N.; Grilo, A.P.; Salles, M.B.C.; Meegahapola, L.; Filho, A.J.S. Primary Frequency Response of Microgrid Using Doubly Fed Induction Generator With Finite Control Set Model Predictive Control Plus Droop Control and Storage System. *IEEE Access* **2020**, *8*, 189298–189312. [CrossRef]
13. Boyle, J.; Littler, T.; Muyeen, S.; Foley, A.M. An alternative frequency-droop scheme for wind turbines that provide primary frequency regulation via rotor speed control. *Int. J. Electr. Power Energy Syst.* **2021**, *133*, 107219. [CrossRef]
14. Mahvash, H.; Taher, S.A.; Rahimi, M.; Shahidehpour, M. Enhancement of DFIG performance at high wind speed using fractional order PI controller in pitch compensation loop. *Int. J. Electr. Power Energy Syst.* **2019**, *104*, 259–268. [CrossRef]
15. Ibrahim, A.O.; Nguyen, T.H.; Lee, D.C.; Kim, S.C. A Fault Ride-Through Technique of DFIG Wind Turbine Systems Using Dynamic Voltage Restorers. *IEEE Trans. Energy Convers.* **2011**, *26*, 871–882. [CrossRef]
16. Zhang, S.; Mishra, Y.; Shahidehpour, M. Fuzzy-Logic Based Frequency Controller for Wind Farms Augmented With Energy Storage Systems. *IEEE Trans. Power Syst.* **2016**, *31*, 1595–1603. [CrossRef]
17. Miao, L.; Wen, J.; Xie, H.; Yue, C.; Lee, W.J. Coordinated Control Strategy of Wind Turbine Generator and Energy Storage Equipment for Frequency Support. *IEEE Trans. Ind. Appl.* **2015**, *51*, 2732–2742. [CrossRef]
18. Mohamed, T.H.; Morel, J.; Bevrani, H.; Hiyama, T. Model predictive based load frequency control_design concerning wind turbines. *Int. J. Electr. Power Energy Syst.* **2012**, *43*, 859–867. [CrossRef]
19. Liu, J.; Yao, Q.; Hu, Y. Model predictive control for load frequency of hybrid power system with wind power and thermal power. *Energy* **2019**, *172*, 555–565. [CrossRef]

20. Abubakr, H.; Vasquez, J.C.; Hassan Mohamed, T.; Guerrero, J.M. The concept of direct adaptive control for improving voltage and frequency regulation loops in several power system applications. *Int. J. Electr. Power Energy Syst.* **2022**, *140*, 108068. [CrossRef]
21. Abubakr, H.; Guerrero, J.M.; Vasquez, J.C.; Mohamed, T.H.; Mahmoud, K.; Darwish, M.M.F.; Dahab, Y.A. Adaptive LFC Incorporating Modified Virtual Rotor to Regulate Frequency and Tie-Line Power Flow in Multi-Area Microgrids. *IEEE Access* **2022**, *10*, 33248–33268.
22. Wu, Z.; Gao, W.; Gao, T.; Yan, W.; Zhang, H.; Yan, S.; Wang, X. State-of-the-art review on frequency response of wind power plants in power systems. *J. Mod. Power Syst. Clean Energy* **2018**, *6*, 1–16. [CrossRef]
23. Dreidy, M.; Mokhlis, H.; Mekhilef, S. Inertia response and frequency control techniques for renewable energy sources: A review. *Renew. Sustain. Energy Rev.* **2017**, *69*, 144–155. [CrossRef]
24. Hwang, M.; Muljadi, E.; Jang, G.; Kang, Y.C. Disturbance-Adaptive Short-Term Frequency Support of a DFIG Associated With the Variable Gain Based on the ROCOF and Rotor Speed. *IEEE Trans. Power Syst.* **2017**, *32*, 1873–1881. [CrossRef]
25. Yang, D.; Gao, H.C.; Zhang, L.; Zheng, T.; Hua, L.; Zhang, X. Short-term frequency support of a doubly-fed induction generator based on an adaptive power reference function. *Int. J. Electr. Power Energy Syst.* **2020**, *119*, 105955. [CrossRef]
26. Margaris, I.D.; Papathanassiou, S.A.; Hatziargyriou, N.D.; Hansen, A.D.; Sorensen, P. Frequency Control in Autonomous Power Systems With High Wind Power Penetration. *IEEE Trans. Sustain. Energy* **2012**, *3*, 189–199. [CrossRef]
27. Liu, T.; Pan, W.; Quan, R.; Liu, M. A Variable Droop Frequency Control Strategy for Wind Farms that Considers Optimal Rotor Kinetic Energy. *IEEE Access* **2019**, *7*, 68636–68645. [CrossRef]
28. Datta, U.; Kalam, A.; Shi, J. Frequency performance analysis of multi-gain droop controlled DFIG in an isolated microgrid using real-time digital simulator. *Eng. Sci. Technol. Int. J.* **2020**, *23*, 1028–1041. [CrossRef]
29. Hwang, M.; Muljadi, E.; Park, J.W.; Sorensen, P.; Kang, Y.C. Dynamic Droop–Based Inertial Control of a Doubly-Fed Induction Generator. *IEEE Trans. Sustain. Energy* **2016**, *7*, 924–933. [CrossRef]
30. Abazari, A.; Monsef, H.; Wu, B. Load frequency control by de-loaded wind farm using the optimal fuzzy-based PID droop controller. *IET Renew. Power Gener.* **2019**, *13*, 180–190. . [CrossRef]
31. Abazari, A.; Dozein, M.G.; Monsef, H. An optimal Fuzzy-logic based frequency control strategy in a high wind penetrated power system. *J. Frankl. Inst.* **2018**, *355*, 6262–6285. [CrossRef]
32. Elyaalaoui, K.; Ouassaid, M.; Cherkaoui, M. Primary frequency control using hierarchal fuzzy logic for a wind farm based on SCIG connected to electrical network. *Sustain. Energy Grids Netw.* **2018**, *16*, 188–195. [CrossRef]
33. Sambariya, D.; Nath, V. Load Frequency Control Using Fuzzy Logic Based Controller for Multi-area Power System. *Br. J. Math. Comput. Sci.* **2016**, *13*, 1–19. [CrossRef] [PubMed]
34. Obaid, Z.A.; Cipcigan, L.; Muhssin, M.T. Fuzzy hierarchal approach-based optimal frequency control in the Great Britain power system. *Electr. Power Syst. Res.* **2016**, *141*, 529–537. [CrossRef]
35. Kayikci, M.; Milanovic, J. Dynamic Contribution of DFIG-Based Wind Plants to System Frequency Disturbances. *IEEE Trans. Power Syst.* **2009**, *24*, 859–867. [CrossRef]
36. Sun, Y.z.; Zhang, Z.s.; Li, G.j.; Lin, J. Review on frequency control of power systems with wind power penetration. In Proceedings of the 2010 International Conference on Power System Technology, Hangzhou, China, 24–28 October 2010; pp. 1–8. [CrossRef]
37. Díaz-González, F.; Hau, M.; Sumper, A.; Gomis-Bellmunt, O. Participation of wind power plants in system frequency control: Review of grid code requirements and control methods. *Renew. Sustain. Energy Rev.* **2014**, *34*, 551–564. [CrossRef]
38. Keung, P.K.; Li, P.; Banakar, H.; Ooi, B.T. Kinetic Energy of Wind-Turbine Generators for System Frequency Support. *IEEE Trans. Power Syst.* **2009**, *24*, 279–287. [CrossRef]
39. Yang, D.; Kim, J.; Kang, Y.C.; Muljadi, E.; Zhang, N.; Hong, J.; Song, S.H.; Zheng, T. Temporary Frequency Support of a DFIG for High Wind Power Penetration. *IEEE Trans. Power Syst.* **2018**, *33*, 3428–3437. [CrossRef]
40. Ali, Y.A.; Ouassaid, M. Advanced Control Strategy of DFIG based Wind Turbine using combined Artificial Neural Network and PSO Algorithm. In Proceedings of the 2020 International Conference on Electrical and Information Technologies (ICEIT), Rabat, Morocco, 4–7 March 2020; pp. 1–7. [CrossRef]
41. Blaabjerg, F.; Xu, D.; Chen, W.; Zhu, N. *Advanced Control of Doubly Fed Induction Generator for Wind Power Systems*; John Wiley & Sons, Inc.: Hoboken, NJ, USA, 2018. [CrossRef]
42. Ali, Y.A.; Ouassaid, M.; Muljadi, E. Reduced Switching Frequency Finite Control Set Model Predictive Control (FCS-MPC) for DFIG. In Proceedings of the 2021 Innovations in Power and Advanced Computing Technologies (i-PACT), Kuala Lumpur, Malaysia, 27–29 November 2021; pp. 1–7. [CrossRef]
43. Yaramasu, V.; Wu, B. *Model Predictive Control of Wind Energy Conversion Systems*, 1st ed.; Wiley: Hoboken, NJ, USA, 2017. [CrossRef]
44. Ekanayake, J.; Jenkins, N. Comparison of the Response of Doubly Fed and Fixed-Speed Induction Generator Wind Turbines to Changes in Network Frequency. *IEEE Trans. Energy Convers.* **2004**, *19*, 800–802. [CrossRef]
45. Mauricio, J.; Marano, A.; Gomez-Exposito, A.; Martinez Ramos, J. Frequency Regulation Contribution Through Variable-Speed Wind Energy Conversion Systems. *IEEE Trans. Power Syst.* **2009**, *24*, 173–180. [CrossRef]
46. Morren, J.; de Haan, S.; Kling, W.; Ferreira, J. Wind Turbines Emulating Inertia and Supporting Primary Frequency Control. *IEEE Trans. Power Syst.* **2006**, *21*, 433–434. [CrossRef]
47. *Model Predictive Control System Design and Implementation Using MATLAB®*; Advances in Industrial Control; Springer: London, UK, 2009. [CrossRef]

48. Kundur, P. *Power System Stability and Control*; McGraw Hill: New York, NY, USA, 1994.
49. Vahidi, B.; Tavakoli, M.; Gawlik, W. Determining Parameters of Turbine's Model Using Heat Balance Data of Steam Power Unit for Educational Purposes. *IEEE Trans. Power Syst.* **2007**, *22*, 1547–1553. [CrossRef]
50. Report, I. Excitation System Models for Power System Stability Studies. *IEEE Trans. Power Appar. Syst.* **1981**, *PAS-100*, 494–509. [CrossRef]
51. Almabrok, A.; Psarakis, M.; Dounis, A. Fast Tuning of the PID Controller in An HVAC System Using the Big Bang–Big Crunch Algorithm and FPGA Technology. *Algorithms* **2018**, *11*, 146. [CrossRef]